Sensitivity analysis of two inverse methods: Beamforming and Bayesian focusing

L Gilquin, Simon Bouley, J. Antoni, T. Le Magueresse, C. Marteau

Sensitivity analysis of two inverse methods: Beamforming and Bayesian focusing

L. Gilquin[a], S. Bouley[a], J. Antoni[a], T. Le Magueresse[b], C. Marteau[c]

[a] *Univ Lyon, INSA-Lyon, Laboratoire Vibrations Acoustique, F-69621 Villeurbanne, France*
[b] *MicrodB, 28 Chemin du Petit Bois, Ecully, France*
[c] *Univ Lyon, Université Claude Bernard Lyon 1, CNRS UMR 5208, Institut Camille Jordan, F-69622 Villeurbanne, France*

Abstract

The characterization of acoustic sources typically involves the retro-propagation of the acoustic field measured with a microphone array to a mesh of the surface of interest, which amounts to solve an inverse problem. Such an inverse problem is built on the basis of a forward model prone to uncertainties arising from mismatches with the physics of the experiment. Assessing the effects of these unavoidable uncertainties on the resolution of the inverse problem represents a challenge. The present paper introduces a practical solution to measure these effects by conducting a sensitivity analysis. The latter provides a mean to identify and rank the main sources of uncertainty through the estimation of sensitivity indices. Two inverse methods are investigated through the sensitivity analysis: Beamforming and Bayesian focusing. The propagation of uncertainties is carried on numerically. The consistency between the real experiment and its numerical simulation is assessed by means of a small batch of measurements performed in a semi-anechoic chamber.

1. Introduction

Numerical models used in various fields (e.g., macroeconomics, fluid dynamics, here acoustics) are often build on large sets of complex equations subject to many sources of uncertainty. This is all the more true for acoustic imaging methods whose aim is to reconstruct acoustic sources through the

Email address: lgilquin@free.fr (L. Gilquin)

resolution of an inverse problem. More specifically, the source reconstruction is achieved by retro-propagating the acoustic field measured with a microphone array to a mesh of the surface of interest. Various methods have been developed throughout the last decades to solve the acoustic inverse problem. A recent classification of these methods has been proposed in [1]. The present papers focuses on two of these methods: conventional Beamforming [2] and Bayesian focusing [3]. The former assumes that the source field to be reconstructed is generated by a finite number of scattered point sources (or monopoles). The latter belongs to the class of "matrix inversion" methods and possesses a wider range of applications as it relaxes the assumption of scattered point sources. In addition, Bayesian focusing brings an unifying framework for acoustic inverse methods, rooted in a Bayesian formalism, that contains as particular cases: ESM [4], HELS [5], NAH [6].

The acoustic inverse problem is built on the basis of a forward model and of the measurements of the acoustic field, prone to sources of uncertainty arising from mismatches with the physics of the experiment. Assessing the effects of these uncertainties on the reconstruction of the source field represents a challenge. In such context, sensitivity analysis (SA) methods are practical tools for studying "how the uncertainty in the output of a model can be apportioned to different sources of uncertainty in the model input" [7]. The main objective of SA is to identity the most contributing inputs variables to an output, i.e., the most important, influential, inputs variables. An auxiliary goal is to detect, within the model, existing interactions between inputs variables. SA methods are commonly classified in three categories: screening, local and global, according to three criteria: their computational cost (number of model evaluations), the complexity of the studied model and the nature of the supplied information.

Historically, SA was conceived and defined only through local methods where the contribution of an input is studied by means of small variations around a nominal value. Such approaches rely on the calculation (or the estimation) of partial derivatives of the model at a specific point [8]. Local methods are however limited by the linearity assumption made on the model and their intrinsic nature (local information). Screening methods are qualitative methods suitable to study sensitivity of models involving several tens to a hundred inputs variables. These methods investigate the contribution of each input only through a few values, yielding a fast but shallow exploration of the model output. The main goal of screening methods is to single out the non-influential inputs variables with a few model calls. The most widely

used screening method is due to [9]. A recent and exhaustive survey of local and screening methods is proposed in [10].

In contrast to both local and screening methods, global SA methods explore sensitivity on the whole variation range of the inputs and produce statistical summaries quantifying the contribution of each input. Examples of statistical summary include: entropy-based indices [11], distribution-based indices [12] and variance-based indices. The present paper focuses on the latter which are based on the functional decomposition of the model output variance [13]. The original approach was introduced by [14] and relies on the calculation of sensitivity measures also known as Sobol' indices. These indices are scalars between zero and one that summarize the influence of each input or combination of inputs. Alternatively, these indices can be interpreted as the share (percentage) of the model variance due to a given input or combination of inputs. In most applications, analytical expressions of Sobol' indices are often inaccessible and one must rely on estimation procedures. Such procedures might be quite expensive, requiring several thousands of model evaluations. To overcome this hindrance, [15] proposed cost-efficient strategies to estimate sets of Sobol' indices at once. Spectral approaches were introduced later on to improve the estimation cost, notably: the FAST method [16], its RBD extension [17] and chaos polynomial-based methods [18].

Coming back to the acoustic inverse problem, only a few applications of SA have been proposed in the literature. In [19], a form of local SA is employed, by means of Taylor series expansions, to study the contributions of sensor and position mismatch to the measured and reconstructed pressures. However, the proposed approach only focuses on main effects and disregards potential interactions. More recently, applications of variance-based methods have been investigated. In [20] and [21], the FAST method is used to perform an SA of respectively an axial fan model and an analytical vibroacoustic transmission model. Even if not being an application of SA, a recent study was proposed in [22] to compare, by means of uncertainty quantification, the robustness of some inverse methods to different sources of uncertainty. To the best of our knowledge, performing a variance based SA of acoustic inverse problems has yet to be addressed. By conducting an SA, the aim of the present paper is to identify and rank the sources of uncertainty altering the resolution of the acoustic inverse problem when either Beamforming or Bayesian focusing is used. The nature of the sources of uncertainty is twofold: the position and orientation of the microphone array, and other sources rel-

ative to the physics of the experiment, namely the ground reflection, the temperature and the signal-to-noise ratio. The propagation of these uncertainties is carried on numerically. Given the relatively small number of inputs and the unknown complexity of the model, Saltelli's procedure is opted for.

This paper is organized as follows. The two investigated inverse formulations, Beamforming and Bayesian focusing, are presented in Section 2. Section 3 provides background on Sobol' indices and reviews Saltelli's estimation procedure. Section 4 presents a numerical application of Saltelli's procedure for the reconstruction of an acoustic source. In addition, a batch of measurements is used to assess the consistency between the real experiment and its numerical simulation.

2. Acoustic inverse problem

2.1. Problem statement

In the frequency domain, the problem of reconstructing an acoustic source is based on a linear relationship between a set of acoustic pressures $\boldsymbol{p}$, measured with a microphone array, and the source field $\boldsymbol{q}$ to be reconstructed. The terms $\boldsymbol{p}$ and $\boldsymbol{q}$ both denote discrete complex quantities. The following set-up is considered to formulate this relationship *at a fixed frequency* f. Denote by $\boldsymbol{r}_i$, $i = 1, \ldots, M$, the microphones positions where the acoustic field is measured. Let Γ be the surface, discretized into a set of points $\boldsymbol{r}$, on which the source field is reconstructed. Then, the linear relationship is completely determined by:

$$p(\boldsymbol{r}_i) = \sum_{\boldsymbol{r} \in \Gamma} G(\boldsymbol{r}_i|\boldsymbol{r}) q(\boldsymbol{r}) + n_i \ , \qquad i = 1, \ldots, M \ , \tag{1}$$

where $G(\boldsymbol{r}_i|\boldsymbol{r})$ denotes the Green function between the surface Γ, at point $\boldsymbol{r}$, and the measurement point $\boldsymbol{r}_i$, and $\boldsymbol{n} = (n_1, \ldots, n_M)$ is the vector of measurement noises. Equation (1) can be rewritten in matrix form to consider all measurements at once:

$$\boldsymbol{p} = \boldsymbol{G}\boldsymbol{q} + \boldsymbol{n} \ . \tag{2}$$

A classical challenge in the acoustic literature is to recover the source field $\boldsymbol{q}$ from (2). This task corresponds to an inverse problem, since one needs to provide an inversion of the operator $\boldsymbol{G}$. Such a problem is typically ill-posed as existence, uniqueness and stability of the solution are not guaranteed. Most of the methods devised to solve this problem, including the ones studied

in this paper, formulate the inverse problem solution through a linear system [3]:

$$\widehat{q}(\boldsymbol{r}) = \sum_{i=1}^{M} a_i(\boldsymbol{r}) \boldsymbol{p}(\boldsymbol{r}_i) \ , \tag{3}$$

where the $a_i(\boldsymbol{r})$ are coefficients that depend on the calculation points $\boldsymbol{r}$. The following two sections focus on the characterization of the solution $\widehat{\boldsymbol{q}}$ when either conventional Beamforming or Bayesian focusing is applied.

2.2. Beamforming

Assuming that the source field can be modeled as a distribution of scattered monopoles, the solution $\widehat{\boldsymbol{q}}$ obtained by conventional Beamforming is based on a component-wise least squares resolution of Eq. (2). The strength of each candidate $\widehat{q}(\boldsymbol{r})$ is estimated independently from the others, as the minimum of the functional:

$$J_{ls}(\boldsymbol{q}) = \|\boldsymbol{G}\boldsymbol{q} - \boldsymbol{p}\|_2^2 \ .$$

In particular:

$$\frac{\partial J_{ls}(\boldsymbol{q})}{\partial q(\boldsymbol{r})^*} = 0 \Leftrightarrow \widehat{q}(\boldsymbol{r}) = \sum_{i=1}^{M} \frac{G(\boldsymbol{r}_i|\boldsymbol{r})^*}{\sum_{k=1}^{M} G(\boldsymbol{r}_k|\boldsymbol{r})^* G(\boldsymbol{r}_k|\boldsymbol{r})} p(\boldsymbol{r}_i) \ ,$$

where the superscript $*$ stands for the conjugate transpose operator. By identification with Eq. (3):

$$a_i(\boldsymbol{r}) = \frac{G(\boldsymbol{r}_i|\boldsymbol{r})^*}{\sum_{k=1}^{M} G(\boldsymbol{r}_k|\boldsymbol{r})^* G(\boldsymbol{r}_k|\boldsymbol{r})} \ , \tag{4}$$

which are the elements of the so-called "steering vector".

2.3. Bayesian focusing

In some acoustic configurations, Beamforming methods might perform poorly. In the low frequency band typically, the hypothesis of uncorrelated source becomes unrealistic, which worsen the spatial resolution of the results. Several alternatives have been proposed in the last decades. This section focuses on a contribution [3] based on Bayesian analysis. The idea is to seek

an optimal interpolation basis that minimizes the reconstruction error of the source field,

$$\widehat{q}(\boldsymbol{r}) = \sum_{k=1}^{P} c_k \phi_k(\boldsymbol{r}) \ , \tag{5}$$

where the c_k are coefficients that depend on the measurements $\boldsymbol{p}(\boldsymbol{r}_i)$ and the ϕ_k are spatial basis functions. Note that this formulation is fully equivalent to Eq. (3), the parallel will be drawn at the end of the section. Substituting Eq. (5) into Eq. (2) leads to:

$$\boldsymbol{p} = \boldsymbol{G\phi c} + \boldsymbol{n} = \boldsymbol{Hc} + \boldsymbol{n} \ , \tag{6}$$

where $\boldsymbol{\phi}$ is the matrix whose columns are the basis functions ϕ_k and $\boldsymbol{c} = (c_1, \ldots, c_P)$ is the vector of coefficients.

Bayesian focusing introduced in [3], builds on such optimality while conjointly incorporating the effects of both noise and prior spatial information, through a Bayesian formulation of the inverse problem. This method has a wider range of applications than Beamforming as it relaxes the assumption of scattered point sources. Bayesian focusing is a "matrix inversion" method that brings a unifying framework for acoustic inverse methods. Through the choice of the basis functions ϕ_k, this framework contains Beamforming, as well as ESM, HELS or NAH as particular cases. The main results of Bayesian focusing are outlined below.

2.3.1. Bayesian framework

Equation (6) is handled within a Bayesian framework, in particular the coefficients c_k are viewed as random variables that produce a random source field $\boldsymbol{q}$. All along this paper, the notation [.] will denote the probability density function of a continuous random variable. The main ingredients of the Bayesian formulation are: the likelihood $[\boldsymbol{p}|\boldsymbol{c}]$ expressing the probability distribution of the measured pressures $\boldsymbol{p}$ given $\boldsymbol{c}$, and the prior probability distribution $[\boldsymbol{c}]$ that incorporates any *a priori* on the source field. Using Bayes' rule, one may express the posterior probability distribution (or posterior) which corresponds to the solution of the inverse problem in the Bayesian setting. This posterior can be viewed as the "inverse probability" of the source field given measurements $\boldsymbol{p}$:

$$[\boldsymbol{c}|\boldsymbol{p}] = \frac{[\boldsymbol{p}|\boldsymbol{c}]\,[\boldsymbol{c}]}{[\boldsymbol{p}]} \propto [\boldsymbol{p}|\boldsymbol{c}]\,[\boldsymbol{c}] \ ,$$

where $\propto$ denotes the "proportional to" symbol. The higher the value of $[\boldsymbol{c}|\boldsymbol{p}]$, the higher the probability that measurements $\boldsymbol{p}$ explain the source field.

2.3.2. MAP estimator

The posterior is viewed as a cost function whose maximization with respect to $\boldsymbol{c}$ will return an optimal solution that most fits the measurements $\boldsymbol{p}$. Consequently, the solution $\widehat{\boldsymbol{c}}$ of Eq. (6) is sought as the maximum *a posteriori* (MAP) estimate:

$$\widehat{\boldsymbol{c}} = \underset{\boldsymbol{c}}{\operatorname{argmax}} \, [\boldsymbol{c}|\boldsymbol{p}] \propto \underset{\boldsymbol{c}}{\operatorname{argmax}} \, [\boldsymbol{p}|\boldsymbol{c}] \, [\boldsymbol{c}] \ . \tag{7}$$

Expressing the MAP estimate requires selecting distributions for both the likelihood $[\boldsymbol{p}|\boldsymbol{c}]$ and the prior $[\boldsymbol{c}]$. Equation (6) states that the likelihood is completely defined by the distribution assigned to the measurement noise $\boldsymbol{n}$. As in [3], here $\boldsymbol{n}$ is assumed to follow a circularly-symmetric complex normal distribution [23]:

$$[n] = \mathcal{CN}(0, \beta^2 \Omega_{\boldsymbol{n}}) \ , \tag{8}$$

where β^2 characterizes the unknown expected noise energy and $\Omega_{\boldsymbol{n}}$ is the covariance matrix, expressing the correlation between the different components of the noise field. As a result, the likelihood follows a circularly complex normal distribution:

$$[\boldsymbol{p}|\boldsymbol{c}] = \mathcal{CN}(\boldsymbol{H}\boldsymbol{c}, \beta^2 \Omega_{\boldsymbol{n}}) \ . \tag{9}$$

The last assumption concerns the prior which is also assumed to follow a circularly-symmetric complex normal distribution:

$$[\boldsymbol{c}] = \mathcal{CN}(0, \alpha^2 \Omega_{\boldsymbol{c}}) \ , \tag{10}$$

where α^2 characterizes the unknown source energy. Injecting (9) and (10) into (7) yields the solution [24]:

$$\widehat{\boldsymbol{c}} = \Omega_{\boldsymbol{c}} \boldsymbol{H}^* (\boldsymbol{H} \Omega_{\boldsymbol{c}} \boldsymbol{H}^* + \eta^2 \Omega_{\boldsymbol{n}})^{-1} \boldsymbol{p} \ , \tag{11}$$

where $\eta^2 = \beta^2/\alpha^2$ identifies as the signal-to-noise ratio (SNR). One may recognize in Eq. (11) the solution of a generalized Thikonov regularization [25] where η^2 plays the role of the regularization parameter. Note that since α^2 and β^2 are unknown variables, the parameter η^2 has to be calibrated. An estimation procedure of η^2, rooted in the posterior distribution, is introduced in [24]. This procedure operates as follows: first the distribution $[\eta^2|\boldsymbol{p}]$ is

obtained by marginalizing the posterior, $[\eta^2|\boldsymbol{p}] = \int [\boldsymbol{c}, \eta^2|\boldsymbol{p}]\,[\boldsymbol{c}]\,d\boldsymbol{c}$. Then, $[\eta^2|\boldsymbol{p}]$ is viewed as a posterior, $[\eta^2|\boldsymbol{p}] \propto [\boldsymbol{p}|\eta^2]\,[\eta^2]$, whose maximization with respect to η^2 yields the regularization parameter.

The choice of the interpolation basis is achieved by considering a singular-value decomposition of $\boldsymbol{G}$ through $\Omega_{\boldsymbol{c}}$ and whitened by the covariance matrix $\Omega_{\boldsymbol{n}}$:

$$\Omega_{\boldsymbol{n}}^{-\frac{1}{2}} \boldsymbol{G} \Omega_{\boldsymbol{c}}^{\frac{1}{2}} = \boldsymbol{U}\boldsymbol{\Sigma}\boldsymbol{V}^* \ ,$$

where $\boldsymbol{\Sigma}$ is a diagonal matrix containing the eigenvalues $s_M \geq s_{M-1} \geq \cdots \geq s_1 \geq 0$. It is proved in [3] that the optimal basis functions ϕ_k, $k = 1, \ldots, P$, are the columns of $\Omega_{\boldsymbol{c}}^{\frac{1}{2}} \boldsymbol{V}$ and that these functions are orthogonal through $\Omega_{\boldsymbol{c}}$. With the interpolation basis and the coefficients (11), the solution of (5) is completely identified with $P = M$, and reads:

$$\widehat{q}(\boldsymbol{r}) = \sum_{k=1}^{M} \frac{s_k}{s_k^2 + \eta^2} \phi_k(\boldsymbol{r}) \boldsymbol{U}_k^* \Omega_{\boldsymbol{n}}^{-\frac{1}{2}} \boldsymbol{p} \ ,$$

where $\boldsymbol{U}_k$ is the k-th column of $\boldsymbol{U}$. Introducing the vector $\widetilde{\boldsymbol{U}}_k = \boldsymbol{U}_k^* \Omega_{\boldsymbol{n}}^{-\frac{1}{2}}$ with elements $\widetilde{U}_{k,i}$, $i = 1, \ldots, M$, the latter expression of $\widehat{q}(\boldsymbol{r})$ can be reformulated as in (3) with:

$$a_i(\boldsymbol{r}) = \sum_{k=1}^{M} \frac{s_k}{s_k^2 + \eta^2} \tilde{U}_{k,i} \ \phi_k(\boldsymbol{r}) \ . \tag{12}$$

Remark that Bayesian focusing admits Beamforming as a limit case when the set of eigenvalues reduces to a singleton, i.e., $s_1 > 0$ and $\forall\ k > 1,\ s_k \approx 0$. Such a phenomenon can occurs, for instance, in far-field acoustic imaging.

2.4. Preliminary observations

Looking at Eqs. (4) and (12) the expressions of the coefficients $a_i(\boldsymbol{r})$ differ between Beamforming and Bayesian focusing. In the former, these coefficients remain unaffected by the sources of uncertainties propagated in the forward problem. In the latter however, the sources of uncertainties have an effect on the coefficients $a_i(\boldsymbol{r})$ through the regularization parameter η^2.

More generally, the two methods differ on the way the source $\boldsymbol{q}$ is reconstructed. Beamforming is classically formulated to retain only the estimated source $\widehat{\boldsymbol{q}}(\boldsymbol{r})$ on the node $\boldsymbol{r}$ where the estimated acoustic strength is maximal (the approach considered in Section 4 will be different). On the other

hand, Bayesian focusing assumes that all nodes of the reconstruction surface are potential radiating point sources. With these two observations in mind, one can expect to observe significant contrasts between the results of the sensitivity analyses performed with each method.

3. Background on Sobol' indices

3.1. Definition of Sobol' indices

Let g represent a deterministic numerical model:

$$\begin{array}{rccc} g & : & K^d & \to & \mathbb{R} \\ & & \boldsymbol{x} = (x_1, \ldots, x_d) & \mapsto & g(\boldsymbol{x}) \ , \end{array}$$

where $\boldsymbol{x}$ is the vector of inputs of g (the sources of uncertainty), d is the dimension of the input space and K^d is a compact subspace of $\mathbb{R}^d$. Let u be a subset of $\mathcal{D} = \{1, \ldots, d\}$, $-u$ its complement and $|u|$ its cardinality. Then, $\boldsymbol{x}_u$ represents a point in $K^{|u|}$ with components $x_j, j \in u$. Given two points $\boldsymbol{x}$ and $\boldsymbol{x}'$, the hybrid point $(\boldsymbol{x}_u : \boldsymbol{x}'_{-u})$ is defined as x_j if $j \in u$ and x'_j if $j \notin u$. $\mathbb{E}[.]$ and $\mathrm{Var}[.]$ denote the expectation and the variance of a random variable.

The uncertainty on $\boldsymbol{x}$ is defined within a probabilistic setting: $\boldsymbol{x}$ is modeled by a vector of independent random variables and is assumed to be uniformly distributed in K^d. For the sake of simplicity, in the following $K^d = [0,1]^d$ [1]. Assume further that $g \in \mathbb{L}^2([0,1]^d, \lambda)$ where λ denotes the Lebesgue measure on $[0,1]^d$. Consider the Hoeffding's decomposition [27, 14] of g:

$$g(\boldsymbol{x}) = g_\varnothing + \sum_{u \subseteq \mathcal{D}, u \neq \varnothing} g_u(\boldsymbol{x}_u) \ . \tag{13}$$

Under the assumptions that $g_\varnothing$ is constant and each term g_u, $u \neq \varnothing$, satisfies:

$$\int_0^1 g_u(\boldsymbol{x}_u) dx_j = 0, \qquad \forall j \in u \ ,$$

the Hoeffding's decomposition becomes unique and $g_\varnothing = \mathbb{E}[g(\boldsymbol{x})] = \mu$. Then, the variance of Eq. (13) leads to the variance decomposition of g:

$$\sigma^2 = \mathrm{Var}[g(\boldsymbol{x})] = \sum_{u \subseteq \mathcal{D}, u \neq \varnothing} \sigma_u^2 \ , \tag{14}$$

[1] The assumption $K^d = [0,1]^d$ is not restrictive, the generalization to other continuous probability distributions can be achieved through many procedures (see [26] for more details)

where $\sigma_u^2 = \mathrm{Var}[g_u(\boldsymbol{x}_u)]$. From this latter decomposition, one can define the two following quantities:

$$\underline{\tau}_u^2 = \sum_{v \subseteq u} \sigma_v^2 \ , \ \overline{\tau}_u^2 = \sum_{v \cap u \neq \varnothing} \sigma_v^2 \ , \ u \subseteq \mathcal{D} \ . \tag{15}$$

Both $\underline{\tau}_u^2$ and $\overline{\tau}_u^2$ satisfy the following relations: $0 \leq \underline{\tau}_u^2 \leq \overline{\tau}_u^2$ and $\underline{\tau}_u^2 = \sigma^2 - \overline{\tau}_{-u}^2$. The definition of Sobol' indices is then obtained by normalizing the two quantities expressed in (15):

$$\underline{S}_u = \underline{\tau}_u^2/\sigma^2 \ , \qquad \overline{S}_u = \overline{\tau}_u^2/\sigma^2 \ , \qquad u \subseteq \mathcal{D} \ . \tag{16}$$

In this paper, only the case $|u| = 1$ is studied. In this context, $\underline{S}_u$ is called first-order Sobol' index and quantifies the main effect of the input x_u on the output $g(\boldsymbol{x})$. Its analogue $\overline{S}_u$ is called total effect Sobol' index and quantifies the main effect of x_u plus the effects of all interactions between x_u and other inputs variables. One may define higher order Sobol' indices but their use is beyond the scope of the present paper.

Sobol' indices enjoy several practical properties. First, their values are scalars varying between zero and one. This yields a straightforward interpretation: the higher the index, the more influential the input. Note that an input is considered as influential if the variance of the output is strongly reduced when this input is fixed. *In particular, it must be stress that Sobol' indices inform by no means directly on the value of the outputs.* Secondly, subtracting the first-order index $\underline{S}_u$ to its counterpart $\overline{S}_u$ returns a direct quantification of all interaction effects between x_u and other inputs. Hence, one may categorize inputs following the nature of their effects: main, interactions, both or none. Third, the following equation can be derived from Eq. (14):

$$\sum_{u \in \mathcal{D}} \underline{S}_u \ + \sum_{u \subseteq \mathcal{D}, u \neq \varnothing, |u| \neq 1} \frac{\sigma_u^2}{\sigma^2} = 1 \ . \tag{17}$$

As a consequence, if the sum of all first-order indices $\underline{S}_u$ is close to one, one can conclude that there exists no interactions between the inputs variables. This last property provides a better understanding of the model behavior.

3.2. Estimation of Sobol' indices

Usually the complexity of the model leads to intractable analytical expressions of Sobol' indices displayed in Eq. (16). In such cases, only approximations of these indices through estimation procedures can be expected.

This section reviews the procedure introduced by Saltelli to estimate both all first-order and all total effect Sobol' indices. This procedure requires the construction of so-called numerical designs of experiments, referred as designs hereafter, to perform evaluations of the model. A design is a point set $\mathcal{P} = \{\boldsymbol{x}_i\}_{i=1}^n$, $\boldsymbol{x}_i = (x_{i,1}, \ldots, x_{i,n}) \in [0,1]^d$, obtained by sampling each input variable x_j n times. It is represented as an $n \times d$ array, where each row corresponds to a point $\boldsymbol{x}_i$ and yields one evaluation of the model $g(\boldsymbol{x}_i)$.

Consider now two designs $\mathcal{P} = \{\boldsymbol{x}_i\}_{i=1}^n$ and $\mathcal{P}' = \{\boldsymbol{x'}_i\}_{i=1}^n$ such that $(\boldsymbol{x}_i, \boldsymbol{x'}_i)$ is uniformly distributed in $[0,1]^{2d}$. One possible way to estimate the two quantities defined in Eq. (15) is:

$$\widehat{\underline{\tau}_u^2} = \frac{1}{n}\sum_{i=0}^{n-1} \left(g(\boldsymbol{x}_{i,u} : \boldsymbol{x'}_{i,-u}) - g(\boldsymbol{x'}_i)\right) g(\boldsymbol{x}_i) \ ,$$

$$\widehat{\overline{\tau}_u^2} = \frac{1}{2n}\sum_{i=0}^{n-1} \left(g(\boldsymbol{x'}_i) - g(\boldsymbol{x}_{i,u} : \boldsymbol{x'}_{i,-u})\right)^2 \ .$$

Then, using an estimator $\widehat{\sigma}^2$ of σ^2 defined as:

$$\widehat{\sigma}^2 = \frac{1}{n-1}\sum_{i=0}^{n-1} \left(g(\boldsymbol{x}_i) - \widehat{\mu}\right)^2 , \ \widehat{\mu} = \frac{1}{n}\sum_{i=0}^{n-1} g(\boldsymbol{x}_i) \ ,$$

the Sobol' indices can be estimated by:

$$\widehat{\underline{S}}_u = \widehat{\underline{\tau}_u^2}/\widehat{\sigma}^2, \qquad \widehat{\overline{S}}_u = \widehat{\overline{\tau}_u^2}/\widehat{\sigma}^2 \ . \tag{18}$$

Based on Eq. (18), the estimation of a single pair $(\underline{S}_u, \ \overline{S}_u)$ requires $3n$ evaluations of the model g. As a result, one would need $3nd$ model evaluations to estimate all first order and total effect indices. To improve this estimation cost, Saltelli introduced in [15, Theorem 1] a subtle estimation strategy based on the following result:

Theorem 1. *The $d+2$ designs $\{\boldsymbol{x}_{i,u} : \boldsymbol{x'}_{i,-u}\}_{i=1}^n$ constructed for $u \in \{\varnothing, \{1\}, \ldots, \{d\}, \mathcal{D}\}$ allow the estimation of all first-order and total effect Sobol' indices at a cost of $n(d+2)$ evaluations of the model.*

Theorem 1 states that there is no need to reevaluate $g(\boldsymbol{x}_i)$ and $g(\boldsymbol{x'}_i)$ for each u. Alternatively, one can simply evaluate $g(\boldsymbol{x}_i)$ n times, $g(\boldsymbol{x'}_i)$ n times, and $g(\boldsymbol{x}_{i,u} : \boldsymbol{x'}_{i,-u})$ nd times, which amounts to a total of $n(d+2)$ evaluations.

The $d+2$ designs of Theorem 1 are obtained by substituting columns of $\mathcal{P}$ for columns of $\mathcal{P}'$ according to u. While elegant, this approach requires a number of model evaluations that grows linearly with respect to d, the input space dimension. However, for applications with a relatively low number of inputs and an affordable computational cost (as in this paper), the number of model evaluations remains reasonable.

4. Application

4.1. Case study

The general set-up that will be studied is presented in Fig. 1-(a). The acoustic source is modeled by a set of 21 correlated monopoles. The closer the monopole to the center of the reconstruction surface Γ, the higher its strength. The aim is to match the acoustic source used in the real experiment. Statistically speaking, each of the 21 monopoles is a random variable:

$$q_k = \sigma_k \times u, \qquad k = 1, \ldots, 21 \ ,$$

where u follows the standard normal distribution $\mathcal{N}(0,1)$ and σ_k characterizes the strength of the monopole. Figure 1-(b) shows a colormap of the values assigned to the σ_k. The dashed black circle outlines the set of 21 monopoles modeling the source.

The microphone array is circular and composed of 36 microphones. Initially, the microphone array is facing towards the reconstruction surface at a distance of 0.6 meters. In the following, this position will be referred as the reference position of the microphone array. The surface of reconstruction Γ is modeled by a rectangular grid, placed in the plane $z = 0.6$, and discretized into 441 points. The ground is modeled by the plane $y = -0.72$.

The measurement noises introduced in Eq. (1) are supposed independent and are each defined by:

$$n_i = 10^{-\mathrm{SNR}/20} \delta_i \mathrm{e}^{\jmath\theta_i} \sqrt{\frac{\|\boldsymbol{p}_0\|_2^2}{M}} \ , \qquad i = 1, \ldots, M \ , \tag{19}$$

where δ_i and θ_i are two independent random variables following respectively a standard normal distribution and a uniform distribution on $[0, 2\pi]$, while $\boldsymbol{p}_0$ is the vector of noise-free pressure.

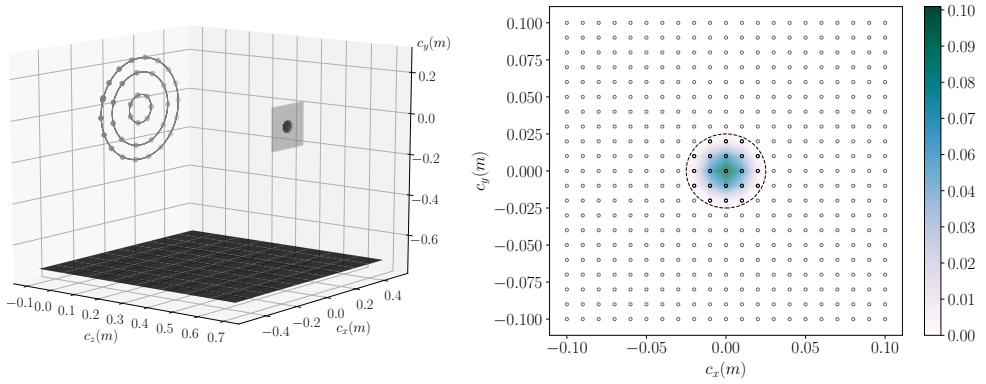

(a) (b)

Figure 1: (color online) (a) Scheme of the study case set-up including: the circular microphone array, the ground, and the reconstruction surface containing the acoustic source. (b) Colormap of the values characterizing the source strength. The dashed circle outlines the set of 21 monopoles (black dots) modeling the source. The nodes of the reconstruction surface are represented by the gray dots.

4.2. Sensitivity analysis setting

4.2.1. Inputs

The sources of uncertainty that will be considered as inputs of the SA are listed in Table 1. The nature of these sources is twofold. Six of them are spatial variables describing the position and orientation of the microphone array: three spatial coordinates c_x, c_y, c_z and three angles $\varphi_x, \varphi_y, \varphi_z$. The remaining three inputs variables gather uncertainties relative to the physics of the experiment, namely: the air temperature T, the SNR and the ground reflection coefficient R. Together, these 9 variables form the vector of inputs $\boldsymbol{x}$ introduced in Section 3.1.

T, SNR and R are uniformly distributed (their ranges are specified in Table 1). The three spatial coordinates c_x, c_y, c_z and the three angles $\varphi_x, \varphi_y, \varphi_z$ all follow truncated normal distributions [28]. The rationale for using truncated normal distributions over normal ones is to discard the tails. The two truncated normal distributions used here are parametrized as follows:

$$\mathcal{TN}_c(0, \sigma_c, -\ell_c, \ell_c) \text{ for } c_x, c_y, c_z, \tag{20}$$

$$\mathcal{TN}_\varphi(0, \sigma_\varphi, -\ell_\varphi, \ell_\varphi) \text{ for } \varphi_x, \varphi_y, \varphi_z \ . \tag{21}$$

inputs	notation	distribution	description
x_1	c_x	$\mathcal{TN}_c$	position x of the array (meters)
x_2	c_y	$\mathcal{TN}_c$	position y of the array (meters)
x_3	c_z	$\mathcal{TN}_c$	position z of the array (meters)
x_4	φ_x	$\mathcal{TN}_\varphi$	angle of rotation about axis x (radians)
x_5	φ_y	$\mathcal{TN}_\varphi$	angle of rotation about axis y (radians)
x_6	φ_z	$\mathcal{TN}_\varphi$	angle of rotation about axis z (radians)
x_7	T	$\mathcal{U}([15, 25])$	air temperature (degrees Celsius)
x_8	SNR	$\mathcal{U}([2, 30])$	signal-to-noise ratio
x_9	R	$\mathcal{U}([0, 1])$	ground reflection coefficient

Table 1: Input variables and their distributions. Symbols $\mathcal{TN}_c$, $\mathcal{TN}_\varphi$ stand for truncated normal distributions whose arguments are specified in Eqs. (20),(21), $\mathcal{U}$ stands for the uniform distribution.

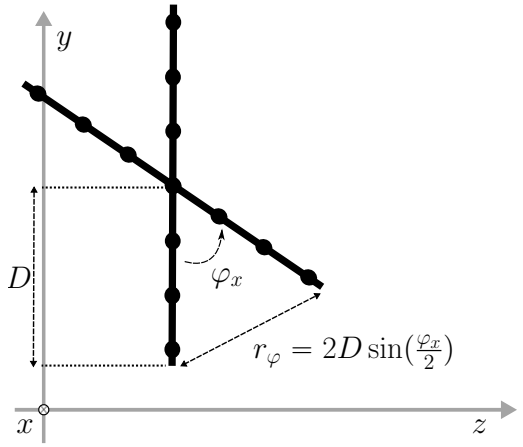

Figure 2: Geometrical interpretation of ℓ_φ with $\varphi = \varphi_x$. r_φ is the chord of φ, D is the radius of the microphone array (in black). Given $D = 0.25\ m$, ℓ_φ is set to be the maximum value of φ such that $r_\varphi = 0.04\ m$.

The parameters ℓ_c, σ_c are the same for the three spatial coordinates c_x, c_y, c_z and likewise for $\ell_\varphi, \sigma_\varphi$ and $\varphi_x, \varphi_y, \varphi_z$. The standard deviations σ_c, σ_φ and bounds ℓ_c, ℓ_φ have been selected to model small position and orientation mismatches that occur when setting a microphone array in an experiment:

$$\ell_c = 0.06,\ \sigma_c = \frac{\ell_c}{q_{0.999}},\ \ell_\varphi = \frac{1}{2}\arcsin\left(\frac{0.04}{2\times 0.25}\right) \approx \frac{9\pi}{180},\ \sigma_c = \frac{\ell_\varphi}{q_{0.999}}\ ,$$

and $q_{0.999}$ is the $99,9\%$ quantile of the standard normal distribution. The

geometrical interpretation of ℓ_φ is sketched in Fig. 2 with $\varphi = \varphi_x$. r_φ denotes the chord of φ, D is the radius of the microphone array. With $D = 0.25\ m$, ℓ_φ is sought as the maximum value of φ such that $r_\varphi = 0.04\ m$. Setting $r_\varphi = 0.04\ m$ ensures the range of variation of the angles $\varphi_x, \varphi_y, \varphi_z$ is similar to those of the spatial coordinates c_x, c_y, c_z.

It is important to point out that the matrices of rotation related to $\varphi_x, \varphi_y, \varphi_z$ do not commute (since $SO(3)$ is a non-commutative group). Here, the sequence of rotations is applied in the following order: $\varphi_x \rightarrow \varphi_y \rightarrow \varphi_z$.

4.2.2. Outputs

Three outputs are selected for the SA: the regularization parameter η^2 (Eq. (11)), a normalized mean square error between cross-spectral matrices and the acoustic power radiated by the reconstructed source field. The last two outputs are investigated with both Beamforming and Bayesian focusing. These two outputs are rooted on quadratic quantities that are often of prime interest in industrial applications. The regularization parameter is interesting to study as it encompasses the effects of the sources of uncertainty on the coefficients $a_i(\boldsymbol{r})$ (Eq. (12)).

The normalized mean square error reads:

$$\text{MSE} = \frac{\|\boldsymbol{S_{pp}} - \boldsymbol{S_{\widehat{p}\widehat{p}}}\|_F}{\|\boldsymbol{S_{pp}}\|_F} \ , \tag{22}$$

where $\boldsymbol{S_{pp}}$ is the cross-spectral matrix of the pressures $\boldsymbol{p}$ obtained after propagating the sources of uncertainty and $\boldsymbol{S_{\widehat{p}\widehat{p}}}$ is the cross-spectral matrix of the pressures obtained from the reconstructed acoustic sources (see Eq. (3)) and propagated without perturbations, that is $\widehat{\boldsymbol{p}} = \boldsymbol{G}\widehat{\boldsymbol{q}}$. The notation $\|.\|_F$ denotes the Frobenius norm. The mean square error assesses whether the acoustic source is well reconstructed or not. Using this output, the SA will inform on the inputs having the most effect on the source reconstruction when their uncertainties are propagated during the forward problem (Eq. (2)).

The last output considered is the acoustic power radiated by the reconstructed source field. The expression of this output varies whether Beamforming or Bayesian focusing is employed. With Beamforming, the acoustic power is taken as the power radiated by the reconstructed source $\widehat{q}$ on the node $\boldsymbol{r}_0$ of Γ where the source strength is maximal (i.e., the center of Γ, $\boldsymbol{r}_0 = (0.0, 0.0, 0.6)$):

$$W_{beam} = \frac{\rho c k^2 |\widehat{q}(\boldsymbol{r}_0)|^2}{8\pi} \ . \tag{23}$$

With Bayesian focusing, the acoustic power consists of summing the power radiated by each virtual source, i.e. each node of Γ, independently and a second term characterizing the influence of the neighbor sources. Formally, this reads:

$$W_{baye} = \sum_{\boldsymbol{r}\in\Gamma} \frac{\rho c k^2 |\widehat{q}(\boldsymbol{r})|^2}{8\pi} + \frac{\mathrm{Re}\{p_{\boldsymbol{r}}\widehat{q}^*(\boldsymbol{r})\}}{2} \ , \tag{24}$$

where $\mathrm{Re}\{.\}$ is the real part operator and $p_{\boldsymbol{r}}$ is the acoustic pressure at position $\boldsymbol{r}$ generated by the other correlated sources:

$$p_{\boldsymbol{r}} = \sum_{\boldsymbol{r}'\in\Gamma\setminus\{\boldsymbol{r}\}} G(\boldsymbol{r}|\boldsymbol{r}')\widehat{q}(\boldsymbol{r}') \ .$$

4.3. Results

Saltelli's procedure is carried on with $n = 10\ 000$ samples of each input variable. The total cost of the procedure corresponds to 110 000 model evaluations. The analysis is conducted for a set of 128 frequencies ranging from 100 Hz to 12 800 Hz with a spacing of 100 Hz. Since the formulation presented in Section 2.1 assumed a fixed frequency, the SA returns one set of Sobol' estimates per frequency. Results are explored with stacked area chart to observe the evolution of the Sobol' estimates in function of the frequency. For each of the three outputs selected, stack area charts of the first-order indices and of the total effect order indices are drawn.

Within Bayesian focusing, the noise covariance matrix $\Omega_{\boldsymbol{n}}$ (Eq. (8)) is chosen to be the identity matrix. The covariance matrix $\Omega_{\boldsymbol{c}}$ (Eq. (10)) is deduced from $\Omega_{\boldsymbol{q}}$ [24, Eq. (6)], the covariance matrix of the prior distribution of the source field. Here, $\Omega_{\boldsymbol{q}}$ is a diagonal matrix whose elements are designed from a two-dimensional Hanning window with radial symmetry and radius 0.05 m.

4.3.1. Regularization parameter

This section displays the results of the SA for the regularization parameter η^2. Figure 3 shows the stacked area chart obtained for the first-order (Fig. 3-a) and the total effect Sobol' estimates (Fig. 3-b).

First, it can be observed that six of the nine inputs have a significant effect on the output: the SNR and R are influential mainly by main effects, the position c_x and c_y of the microphone array are influential mainly by interactions, the angles φ_x and φ_y are influential by both main effects and interactions.

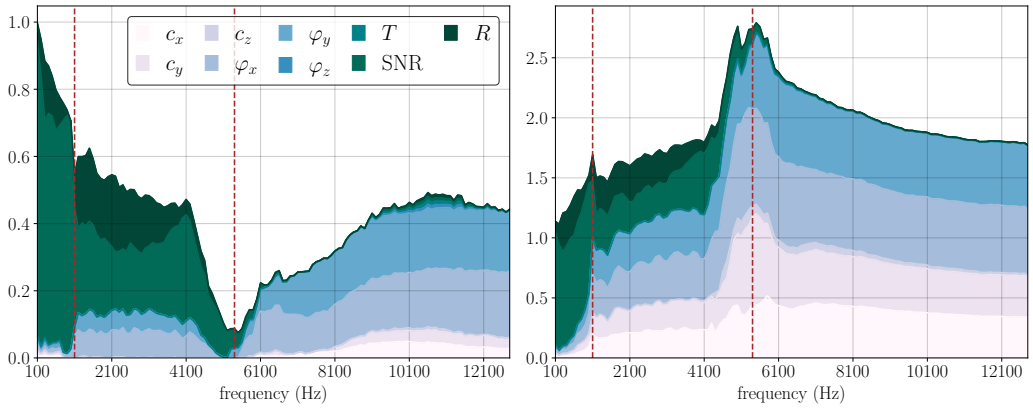

(a) (b)

Figure 3: (color online) Stack area charts for the regularization parameter η^2. (a) First-order Sobol' indices. (b) Total effect Sobol' indices.

The second observation focus on the behavior of the output η^2. The two vertical dashed lines indicate respectively the low cutoff frequency, $f_{lc} \approx 1000$ Hz, and high cutoff frequency of the microphone array, $f_{hc} \approx 5000$ Hz. These frequencies mark a transition between uncertainties due to the propagation model and uncertainties due to the position and orientation of the microphone array. Up to f_{lc}, only SNR and R are influential, that is only uncertainties due to the propagation model affect η^2. From f_{lc} to f_{hc} the effects of SNR and R progressively decrease while those of c_x, c_y, φ_x and φ_y increase. From f_{hc} onward, SNR and R stop being influential and only the uncertainties about the position and the orientation of the antenna affect η^2.

As a final observation, the sum of the first-order indices is always lower than 0.5 from 3000 Hz onward. This shows the importance of the interaction effects on the parameter η^2.

4.3.2. Mean square error

This section displays the results of the SA for the mean square output defined in Eq. (22). Figure 4 shows the stacked area chart obtained with Beamforming (Figs. 4-a, 4-b) and Bayesian focusing (Figs. 4-c, 4-d).

From a qualitative point of view, the stack area charts obtained with Beamforming or Bayesian focusing allow the identification of the same subset of influential inputs: R, c_x, c_y, φ_x, φ_y. The nature of their effects is the same as in the study conducted on η^2, that is: R is influential mainly by main

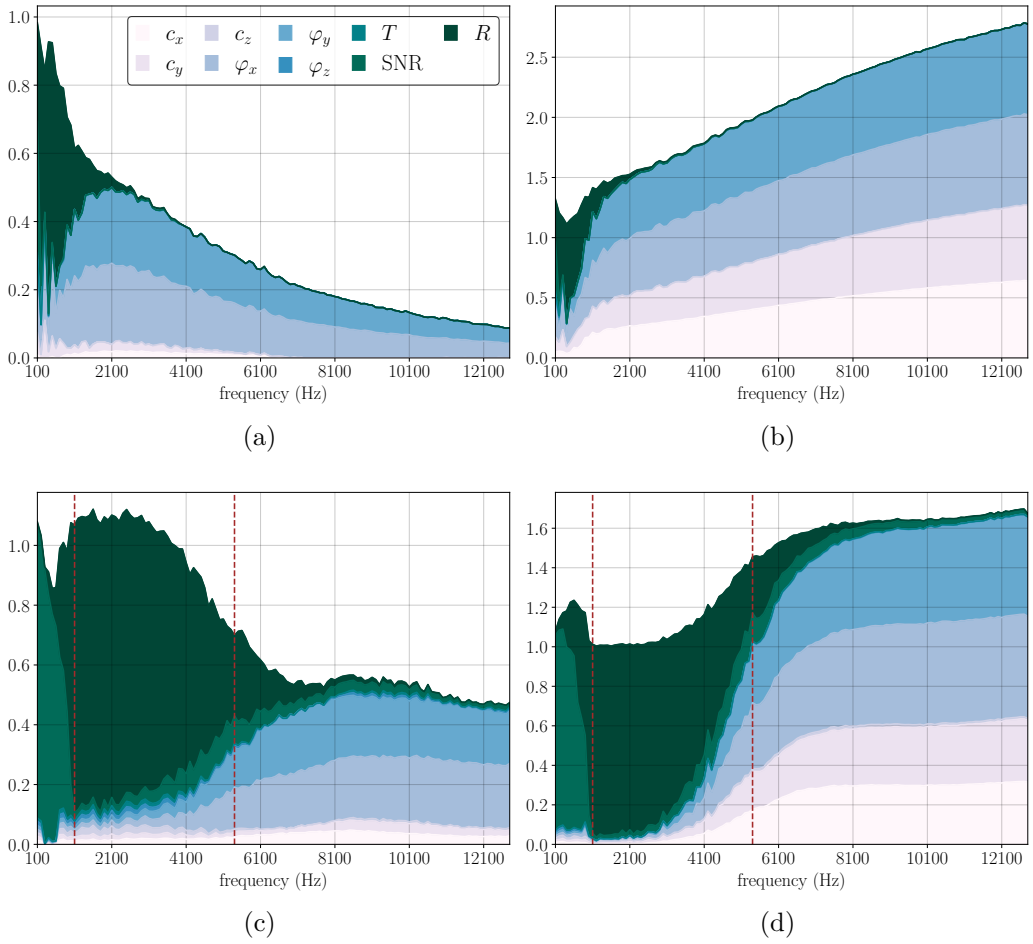

Figure 4: (color online) Stack area charts for the MSE with Beamforming: (a) first-order Sobol' indices, (b) total effect Sobol' indices, and with Bayesian focusing: (c) first-order Sobol' indices, (d) total effect Sobol' indices.

effect, c_x, c_y mainly by interactions and φ_x, φ_y by both. The only exception is the SNR captured with Bayesian focusing alone. This is not unforeseen as the Bayesian formulation, reviewed in Section 2.3.2, specifically accounts for the noise effect through the covariance matrix $\Omega_{\boldsymbol{n}}$.

From a quantitative point of view however, the results differ between Beamforming and Bayesian focusing. The SNR and R are influential on a much wider frequency band with Bayesian focusing: from 100 to 7000 Hz against 100 to 1000 Hz with Beamforming. This shows that, in terms of

mean square error, Beamforming is more robust to "model" uncertainties than Bayesian focusing.

Such a discrepancy can easily be explained. As discussed in Section 2.4, with Beamforming, the reconstructed source $\widehat{\boldsymbol{q}}$ (Eq. (3)) is only affected by the uncertainties through $\boldsymbol{p}$. With Bayesian focusing instead, $\widehat{\boldsymbol{q}}$ is not only affected by these uncertainties, but also by those through η^2 as seen in Eq. (12). Yet the previous SA of η^2 highlighted the influence of SNR and R up to roughly 5000 Hz. This explains why these two parameters possess a wider frequency range of influence with Bayesian focusing, and also why similar transitions to those highlighted in the study of η^2 can be observed.

To conclude this analysis, one may observe in Figs. 4-a and 4-c a progressive decrease of the sum of the main effects (conversely an increase of the interaction effects). This outlines again the importance of the interactions between inputs modeling the position and orientation of the microphone array.

4.3.3. Acoustic power

This section displays the results of the SA for the acoustic power defined in Eqs. (23) and (24). Figure 5 shows the stacked area chart obtained with Beamforming (Figs. 5-a, 5-b) and Bayesian focusing (Figs. 5-c, 5-d).

Unsurprisingly, the results obtained with both methods are drastically different. This is simply due to the formulation of the acoustic power contrasting between the two approaches. With Beamforming, six influential inputs are identified: c_x, c_y, c_z, φ_x, φ_y and R. The inputs c_z and R are influential by main effects and only in the low frequency band, c_x, c_y are influential by interactions and φ_x and φ_y by both. The influence of c_z is most likely due to the acoustic power decreasing as $1/D^2$ in low frequencies where D is the distance between a microphone and a node of the reconstruction surface.

With Bayesian focusing, seven inputs are influential: c_x, c_y, φ_x, φ_y, T, SNR and R, all by both main effects and interactions over the whole frequency range. The exception is the temperature T, influential only in the low frequency band. The effect of the temperature stems from the second term of W_{baye} (Eq. (24)) that accounts for the pressure generated by neighbor sources. Once more, the low cutoff frequency of the microphone array indicates transitions, although different from those observed in the last two studies. Up to f_{lc}, only SNR, R and T are influential. Then, from f_{lc} onward, the effects of c_x, c_y, φ_x, φ_y, SNR and R progressively grow.

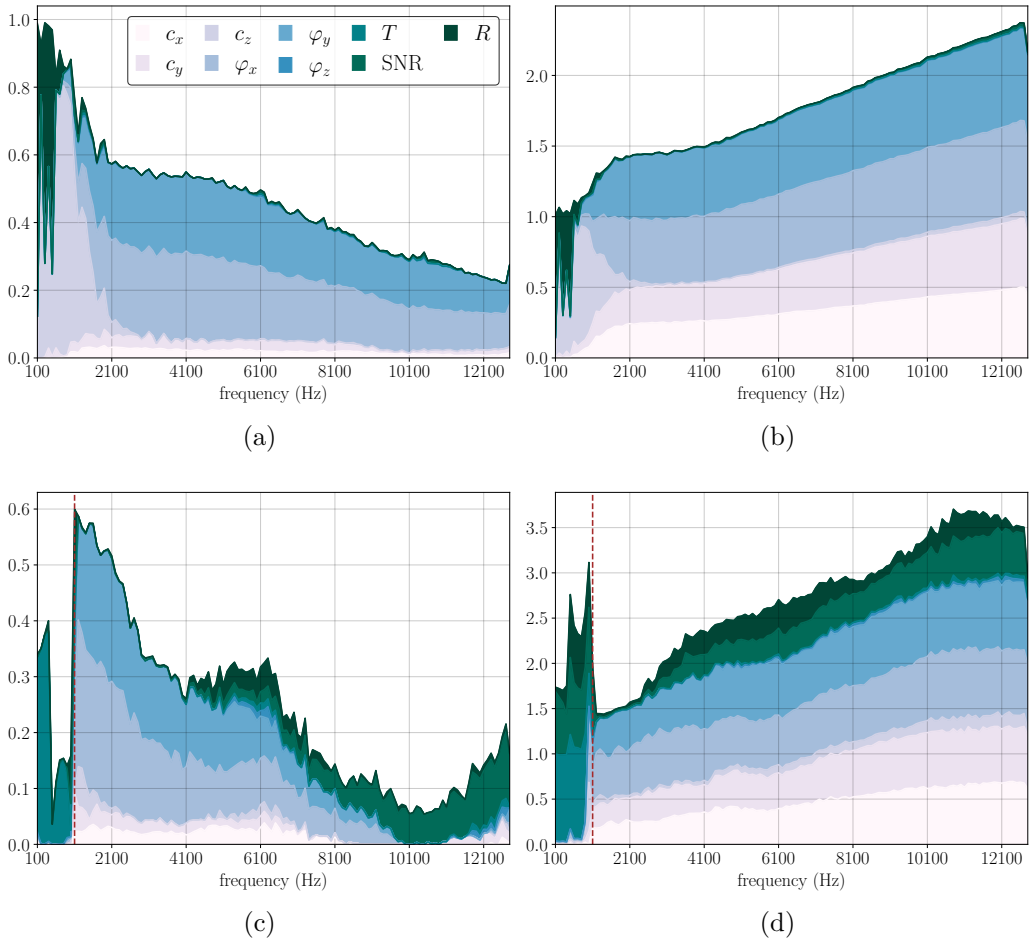

Figure 5: (color online) Stack area charts for the acoustic power with Beamforming (W_{beam}) : (a) first-order Sobol' indices, (b) total effect Sobol' indices, and with Bayesian focusing (W_{baye}): (c) first-order Sobol' indices, (d) total effect Sobol' indices.

The results for both methods highlight once again the importance of the interaction effects between inputs modeling the position and orientation of the microphone array.

4.3.4. Additional remarks

Among the three SA performed, the input φ_z is the only one to never be influential. This was predictable given the geometry of the set-up: a rotation of angle φ_z about the z axis leaves the microphone array in the same plane

(i.e. the circular array revolves around axis z), parallel to the reconstruction surface.

The results of the SA underline the complexity of acoustic imaging: important variations of the Sobol' indices with the frequency in addition to the predominance of interaction effects (in most numerical models it is generally the main effects that drive the variance of the output). All three outputs studied point out the effects of interactions between inputs modeling the position and the direction of the microphone array. Hence, the array should be set with utmost care before conducting and experiment.

As a conclusive remark, one should pay attention that the SA performed here is dependent of many factors: the number of inputs, the distributions assigned to the inputs, the nature of the output selected, the configuration of the set-up (number of microphones, number of sources, geometry of the microphone array and so on). Consequently, the conclusions drawn for this particular set-up cannot be easily generalized to other case studies.

4.4. Comparison with real measurements

This section provides a comparison between the real experiment, using a batch of measurements conducted in a semi-anechoic chamber, and its numerical approximation. Due to material constraints, only four of the nine parameters listed in Table 1 were used in the real experiment: the positions c_x, c_y, c_z of the microphone array and the ground reflection R. The effect of the ground reflection was captured by the addition or subtraction of an absorbent foam on the ground. This constrains R to be modeled as a bimodal variable. A total of 8 experiments were conducted by varying the four inputs at once.

The adequation between the real experiment and its numerical approximation is gauged by checking if the real output values (obtained with the real experiments) fall far from the distribution of the numerical outputs. The adequation is analyzed for the two outputs: MSE and acoustic power level, and with the two inverse methods: Beamforming and Bayesian focusing. The acoustic power levels are derived from Eqs. (23) and (24) by:

$$L_{W_{beam}} = 10\log_{10}\left(\frac{W_{beam}}{10^{-12}}\right) , \qquad L_{W_{baye}} = 10\log_{10}\left(\frac{W_{baye}}{10^{-12}}\right) .$$

The sampling used in Saltelli's procedure enables the computation of some statistical features characterizing the output distribution. These features

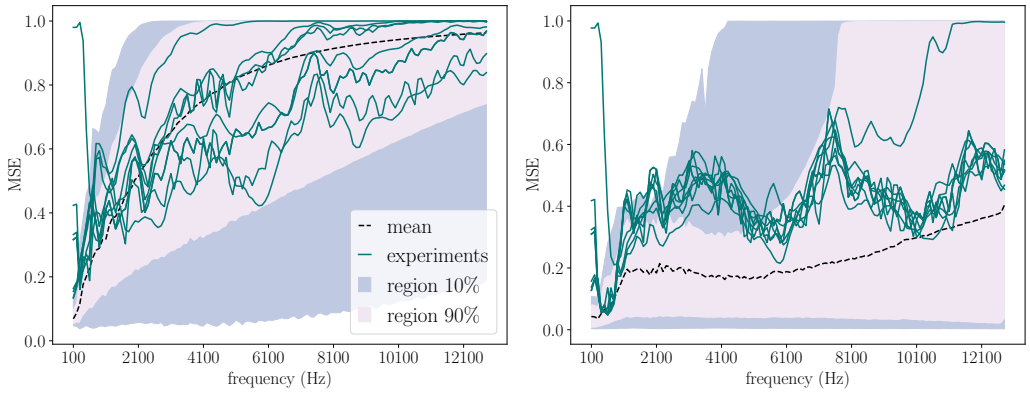

Figure 6: (color online) Distribution of the output MSE when the acoustic source is reconstructed with either: (a) Beamforming or (b) Bayesian focusing. The two regions are delimited by the fifth and the 95-th percentiles of the numerical outputs.

can be exploited in turns, and in parallel with the results of the sensitivity analysis, to draw further conclusions. The features selected here are the mean and the fifth and 95-th percentiles. In Figures (6) and (7), the mean is displayed as a dashed curve, the fifth and the 95-th percentiles delimit two regions: one encompassing 90% of the numerical values, the other containing the remaining 10%.

4.4.1. Mean square error

Figure 6-(a) shows the values of the MSE when the source $\boldsymbol{q}$ is reconstructed with Beamforming. It can be seen that the real outputs match well with the distribution of the numerical outputs. The real outputs all spread inside the region containing 90% of the values. The mismatch observed in the very low frequency band (below 500 Hz) is most likely due to the Beamforming method itself, known to perform poorly in this frequency range.

Results shown on Fig. 6-(b), when the source $\boldsymbol{q}$ is reconstructed with Bayesian focusing, are more mitigated. Up to 5000 Hz, the real outputs fall almost all within the region containing 10% of the values. From 5000 Hz onward, the real outputs fall within the 90% region but are still far from the mean curve. The origin of the discrepancy observed up to 5000 Hz presumably follows from the presence of other sources of uncertainty that were not accounted for in the numerical model (*e.g.* diffraction or reflection

on objects in the chamber during the experiment). The results presented in Figs. (4)-(c) and (4)-(d)) back up this assertion. It was revealed that up to the frequency 5000 Hz, the MSE is mainly affected by source of uncertainties inherent to the propagation model (SNR and R).

Looking at the distribution of the numerical outputs, Bayesian focusing is clearly more resilient to uncertainties than Beamforming, both in terms of mean and 90% region. With Bayesian focusing, the MSE starts worsening around the high cutoff frequency of the antenna, which corresponds to the frequency where the parameters describing the position and orientation of the antenna start being influential (see Figs. (4)-(c) and (4)-(d)). The observation is identical with Beamforming, the MSE progressively worsen as the effects of these parameters grow. From these observations, it can be concluded that the effects of these parameters are those altering the most the resolution of the inverse problem, while the effects of the SNR and the ground reflection are less pronounced.

4.4.2. Acoustic power level

For the results presented in this section, the values of the acoustic power level computed numerically were adjusted to match the order of magnitude of the acoustic power level obtained from the real experiments.

Fig. 7-(a) shows the values of the acoustic power level when the source $\boldsymbol{q}$ is reconstructed with Beamforming. Again, the real outputs match well with the distribution of the numerical outputs. The real outputs are more concentrated in the upper half of the 90% region. The results highlight the interaction effects, taking place from 2000 Hz onward and lessening the power level.

Figure 7-(b) shows the values of the acoustic power level when the source $\boldsymbol{q}$ is reconstructed with Bayesian focusing. The real outputs match particularly well with the distribution of the numerical outputs. The experiment curves are spread close to the mean in the low and high frequency bands. In contrast to Beamforming, the interaction effects can diminish as much as increase the power level. The rationale for such a result most probably comes from the additional term in W_{baye} (Eq. (24)).

Concerning the distribution of the numerical outputs, the conclusions are identical to those drawn in the previous section. The acoustic power level worsen in the frequency band where the effects of the parameters related to the position and the orientation of the antenna prevail. Furthermore, Bayesian focusing appears to be more resilient once again.

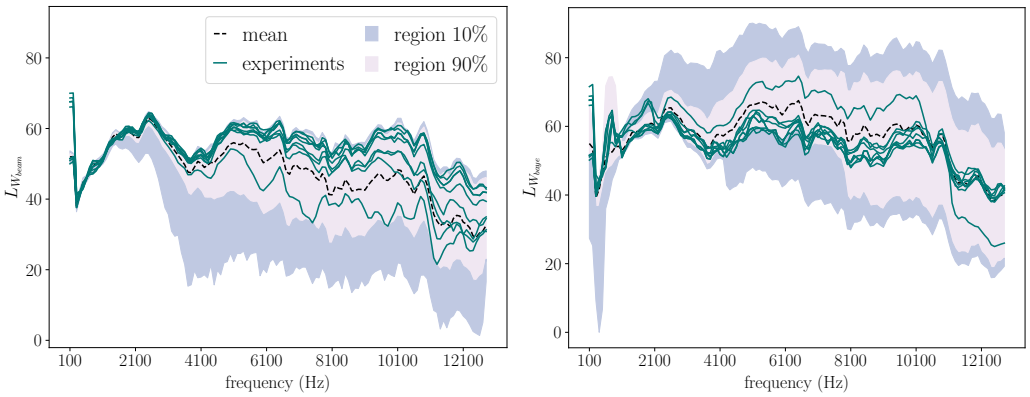

(a) (b)

Figure 7: (color online) Distribution of the acoustic power level when the source is reconstructed with either: (a) Beamforming or (b) Bayesian focusing. The two regions are delimited by the fifth and the 95-th percentiles of the numerical outputs.

4.4.3. Conclusive remarks

The distribution of the numerical outputs shown in Fig. 6 and Fig. 7 might seem extreme. However, this can easily be explained by the wide range of variations selected for the study performed in this paper, in particular for the position and orientation of the antenna. Smaller ranges would lead to tighter 90% and 10% regions.

On the other hand, one may wonder why the experimental curves are not scattered inside the 90% region. This can be explained by the three angles characterizing the microphone array orientation, whose effects were not consider in the real experiments due to logistic constraints. The importance of these parameters have been highlighted in all the SA conducted as much as in the quantitative studies of Section 4. By not including these parameters, the variation of the different outputs is greatly reduced and the experimental curves are close to each others.

As a final note, an equivalent analysis was conducted for η^2 with matching results as well, although not presented here due to lack of space.

5. Conclusion

The sensitivity analysis method based on the calculation of Sobol' indices has been employed in this paper to study the effect of uncertainties on the

reconstruction of an acoustic source. Two inverse methods have been investigated for the reconstruction: Beamforming and Bayesian focusing. The sources of uncertainty that have been considered are spatial variables describing the position and orientation of the microphone array and variables relative to the physics of the experiment: temperature, ground reflection and SNR. The SA has been performed for the following outputs: a normalized mean square error between cross-spectral matrices, the acoustic power radiated by the reconstructed source field and the regularization parameter of the Bayesian approach.

All in all, both the results of the SA and the studies of the outputs distributions have pointed out the importance of the effects of the parameters modeling the position and the direction of the microphone array. From an experimental point of view, this suggests that the main effort should be focused on properly setting the microphone array. The SA results also backed up the assertion that Beamforming and Bayesian focusing differ drastically. From a qualitative point of view, the subset of influential parameters are not identical. Quantitatively speaking, while the nature of the influences (interactions and/or main effects) have been found similar with both formulations, the frequency range of each influential input is contrasted.

The results of the real experiments conducted in the semi-anechoic chamber have agreed quite well with the numerical model. The slight discrepancies observed most probably stem from other sources of uncertainty that were not considered in the SA or from the method itself (e.g., Beamforming known to perform badly in the low frequency band). Bayesian focusing was also shown to be overall more resilient than Beamforming to the sources of uncertainty.

Acknowledgments

This work was supported by the LUG2 project funded by the Région Auvergne Rhône-Alpes and the BPIFrance (grant FUI22). This work was performed within the framework of the Labex CeLyA of Université de Lyon, operated by the French National Research Agency (ANR-10-LABX-0060/ANR-11-IDEX-0007).

References

[1] Q. Q. Leclère, A. Pereira, C. Bailly, J. Antoni, C. Picard, A unified formalism for acoustic imaging based on microphone array measurements, International Journal of Aeroacoustics 16 (4-5) (2017) 431–456.

[2] J. Billingsley, R. Kinns, The acoustic telescope, J. Sound Vib. 48 (4) (1976) 485–510.

[3] J. Antoni, A bayesian approach to sound source reconstruction: Optimal basis, regularization, and focusing, J. Acoust. Soc. Am. 131 (4) (2012) 2873–2890.

[4] A. Sarkissian, Extension of measurement surface in near-field acoustic holography, J. Acoust. Soc. Am. 115 (4) (2004) 1593–1596.

[5] S. F. Wu, On reconstruction of acoustic pressure fields using the helmholtz equation least squares method, J. Acoust. Soc. Am. 107 (5) (2000) 2511–2522.

[6] E. G. Williams, Fourier Acoustics: Sound Radiation and Nearfield Acoustical Holography, Academic Press, London, 1999.

[7] A. Saltelli, K. Chan, E. M. Scott, Sensitivity Analysis, Wiley, 2008.

[8] H. Rabitz, Systems analysis at the molecular scale, Science 246 (1989) 221–226.

[9] M. D. Morris, Factorial sampling plans for preliminary computational experiments, Technometrics 33 (2) (1991) 161–174. doi:10.2307/1269043.

[10] B. Iooss, P. Lemaître, A review on global sensitivity analysis methods, in: Uncertainty management in Simulation-Optimization of Complex Systems: Algorithms and Applications, Springer, 2015.

[11] H. Liu, W. Chen, A. Sudjianto, C. Wei, Relative entropy based method for probabilistic sensitivity analysis in engineering design, J. Mech. Des 128 (2) (2005) 326–336.

[12] E. Borgonovo, A new uncertainty importance measure, Reliab. Eng. Syst. Saf. 92 (6) (2007) 771–784. doi:10.1016/j.ress.2006.04.015.

[13] B. Efron, Nonparametric standard errors and confidence intervals, Can. J. Stat. 9 (2) (1981) 139–158.

[14] I. M. Sobol', Sensitivity indices for nonlinear mathematical models, Mathematical Modeling and Computational Experiment 1 (1993) 407–414.

[15] A. Saltelli, Making best use of models evaluations to compute sensitivity indices, Comput. Phys. Commun. 145 (2) (2002) 280–297.

[16] A. Saltelli, S. Tarantola, K.-S. Chan, A quantitative model-independent method for global sensitivity analysis of model output, Technometrics 41 (1) (1999) 39–56.

[17] S. Tarantola, D. Gatelli, T. A. Mara, Random balance designs for the estimation of first order global sensitivity indices, Reliab. Eng. Syst. Saf. 91 (6) (2006) 717–727.

[18] B. Sudret, Global sensitivity analysis using polynomial chaos expansions, Reliab. Eng. Syst. Saf. 93 (7) (2008) 964–979.

[19] K.-U. Nam, Y.-H. Kim, Errors due to sensor and position mismatch in planar acoustic holography, J. Acoust. Soc. Am. 106 (4) (1999) 1655–1665.

[20] H. Trabelsi, M. Abid, M. Taktak, T. Fakhfakh, M. Haddar, Effect of the aerodynamic force modeling on the tonal noise prediction model for axial fan: Sensitivity and uncertainty analysis, Applied Acoustics 117 (Part A) (2017) 61 – 65.

[21] J.-L. Christen, M. Ichchou, B. Troclet, O. Bareille, M. Ouisse, Global sensitivity analysis and uncertainties in sea models of vibroacoustic systems, Mech. Syst. Signal Pr. 90 (Supplement C) (2017) 365–377.

[22] E. Sarradj, G. Herold, S. Jekosch, Array methods: Which one is the best?, in: Proceedings of the 7th Berlin Beamforming Conference, 2018.

[23] R. A. Wooding, The multivariate distribution of complex normal variables, Biometrika 43 (1-2) (1956) 212–215.

[24] A. Pereira, J. Antoni, Q. Leclère, Empirical bayesian regularization of the inverse acoustic problem, Applied Acoustics 97 (Supplement C) (2015) 11–29.

[25] P. Hansen, Rank-Deficient and Discrete Ill-Posed Problems, Society for Industrial and Applied Mathematics, 1998. doi:10.1137/1.9780898719697.

[26] L. Devroye, Non-Uniform Random Variate Generation, Springer-Verlag, New York, 1986.

[27] W. F. Hoeffding, A class of statistics with asymptotically normal distribution, Ann. Math. Stat. 19 (3) (1948) 293–325.

[28] N. L. Johnson, S. Kotz, N. Balakrishnan, Continuous Univariate Distributions, Volume 1, 2nd Edition, Wiley, 1994.